Analysis of the riveting process forming mechanisms

Eric Markiewicz, Bertrand Langrand, Eric Deletombe, Pascal Drazetic, Laurent Patronelli

Analysis of the riveting process forming mechanisms

E. Markiewicz, B. Langrand*, E. Deletombe,*
P. Drazetic and L. Patronelli*

Industrial and Human Automatic Control and Mechanical Engineering Laboratory, Mechanical Engineering Research Group (URA CNRS D1775), University of Valenciennes - Le Mont Houy, B.P. 311, 59304 Valenciennes Cedex, France
E-mail: markiewicz@univ-valenciennes.fr

* ONERA-Lille, Solid and Damage Mechanics Department, Structural Resistance and Design Section, 5, Bvd Paul Painlevé - 59000 Lille, France
E-mail: langrand@imf-lille.fr

Abstract: This paper deals with the characterisation of the residual stresses and strains due to the riveting process. In the first part, experimental results are given for two metal plate geometries and for three aspect ratios a/ϕ (edge margin/rivet shank diameter). As a result of this experimental investigation, a detailed analysis of forming and placing mechanisms is described for one rivet. Results show that the riveting process can be divided into seven distinct steps. The second part deals with the simulation capability by explicit FE codes, such as Pam-Solid™, to represent the local plastic flow along the riveting process. FEM results prove the numerical tool's ability to represent this complex forming process. FEM numerical tools can therefore optimize rivet designs more quickly and cheaply than experiments.

Keywords: experimentation, finite element simulation, forming mechanisms, riveted joints.

Reference to this article should be made as follows: Markiewicz, E., Langrand, B., Deletombe, E., Drazetic, P. and Patronelli, L. (1998) 'Analysis of the riveting process forming mechanisms', *Int. J. of Materials and Product Technology*, Vol. 13, Nos 3–6, pp. 123–145.

Notation

a edge margin

e metal plate thickness

h_{bout} driven head height

j gap between rivet and punching

p pitch

A, B, n identified parameters of constitutive model (power model)

E Young's modulus

G shear modulus

K bulk modulus

L length (or diameter) of the residual specimens

L_R length of the rivet

L_{TI} length (or diameter) of the residual specimens fixed by calculation rules

δ_j gauge distance from the punching edge

ε_{max} maximum metal plate strain

ε_p true plastic strain

ε_{res} residual (or post-riveting) metal plate strain

ϕ rivet shank unbuckled diameter

ϕ_{imp} rivet driven head diameter

ϕ_{max} maximum rivet driven head diameter

ν Poisson's ratio

σ true stress

1 Introduction

The finite element modelling of quasi-static or dynamic behaviour for complex aeronautical frameworks gives rise to very large numerical models. The numerical tools, although they are becoming more and more powerful, still cannot handle the suitable number of finite elements needed for the simulation of all the nonlinear phenomena met in crash or impact problems. The most recent numerical results [1, 2] have shown that the main problem with FE simulations comes from the poor representation of the influence of the riveting.

One of the most important unresolved aspects concerns the influence of material embrittlement due to the punching and riveting process. This embrittlement leads, in the highest stressed area, to fundamental differences between real and numerical behaviour. This joining method is based on the crushing of a body (the rivet) which is constrained to remain in a confined space (the punching) to compose a physical link between two components. The strength of such a joint depends therefore on the local initial stress state.

How important is this influence? Similarly, how are these initial stresses set into the metal plates? To evaluate an ideal strain gradient along the metal plates the riveting should be carried out with an isotropic and infinite environment. A circular metal plate

geometry seems to be appropriate to verify an isotropic strain distribution. Geometric or corner effects can be evaluated by square metal plate geometry specimens.

The main aim of this paper is to determine the residual or post-riveting strain cartography according to the aspect ratio between the punching radius $\phi/2$ and the specimen dimensions, and then to study the influence of this ratio on the metal plate strain distribution and to study the influence of the specimen geometry (corner effects). A secondary aim is to accurately model the joint and evaluate the simulation capability by explicit FE codes, such as PAM-SOLID™, to represent the local material forming due to the riveting. This study is part of a current research programme which concerns the characterisation of riveted assemblies under dynamic conditions of loading. This is why an explicit FE code has been chosen.

2 Experiment

Experiments are carried out on elementary specimens, Figure 1:

(i) one 7050 aluminium alloy countersunk rivet:

- shank diameter: $\phi = 4$ mm,
- initial length: $L_R = 8$ mm,

(ii) two 2024-T351 aluminium alloy plates:

- thickness: $e = 1.6$ mm.

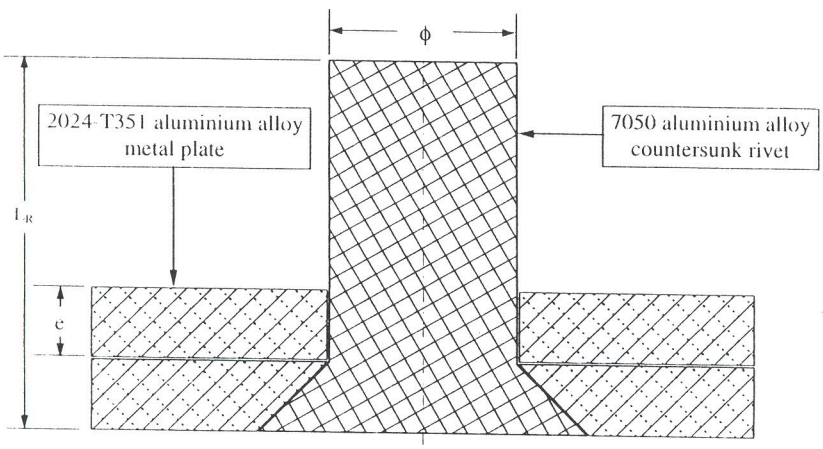

Figure 1 *Elementary residual stress specimen.*

The norm recommends a minimum margin between the rivet and the metal plate edge, a (edge margin) or between two rivets, p (pitch). These values are defined from calculation rules [3] or tables [4, 5] and determine the reference case (L_{TI}). Different configurations are tested to measure the influence of the pitch or the edge margin on the range and the distribution of the residual strains due to the joining method.

Three cases are set-up:

(i) $L > L_{TI}$: to break edge effects,

(ii) $L = L_{TI}$: the nominal case given by the standard calculation rules [3],

(iii) $L < L_{TI}$: a critical case.

For each dimension two metal plate geometries are tested:

(i) a circular one: to secure an isotropic strain distribution and to measure edge effects,

(ii) a square one: to measure corner effects.

The different configurations are summarised in Table 1.

Table 1 Test configurations.

Type	Case	L (mm)	ϕ_f (mm)
Square	$L > L_{TI}$	20	4
	$L = L_{TI}$	15	4
	$L < L_{TI}$	10	4
Circular	$L > L_{TI}$	20	4
	$L = L_{TI}$	15	4
	$L < L_{TI}$	10	4

2.1 *Experimental set-up*

The residual strain specimens were prepared by the DASSAULT AVIATION company. Punchings were drilled in industrial ways. The dimensions of the straight and countersunk punchings were based on the DASSAULT AVIATION company's manufacturing norms for a 4 mm diameter countersunk rivet. Punching plates were cut at ONERA-Lille with electroerosion machining (Figure 2). The rivet is called 'permanent' because the installation delay is much longer than for the so-called 'soaking rivet'. These permanent rivets are increasingly used to join aeronautical frameworks because of this installation flexibility.

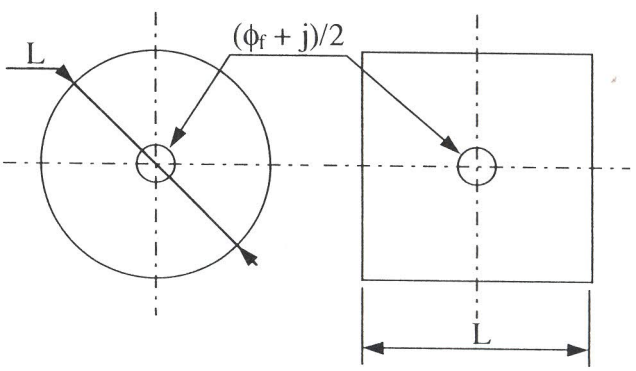

Figure 2 *Specimens shape.*

The riveting was processed on an INSTRON 1195 quasi-static tension/compression machine. The riveting velocity was quasi-static: 2 mm/min. Figure 3 presents the experimental set-up. The test consists in:

(i) a crushing step,

(ii) a stress homogenization step,

(iii) a relaxation step.

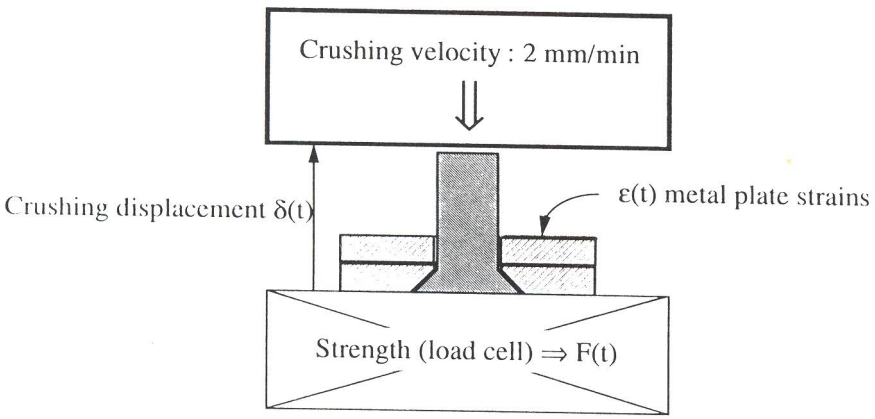

Figure 3 *Experimental set-up.*

The riveting was standardised by geometrical criteria for the strain level and the volume of the rivet driven head [6]. Micro-gauges were chosen to fit out the metal plates of the residual stress specimens (Vishay ref. EA06-015EH120 and EP08-015CK120) although there are strain visualisation methods such as Moiré [7] or Speckle [8]. Gauges were stuck on the specimens with respect to median and diagonal directions (Figure 4). The gauge numbering between each specimen did not correspond because the specimens were different lengths.

However, for circular metal plate specimens, gauges 1-5 were stuck on the metal plate with respect to the median direction. The spacing between two consecutive gauges was 1.5 mm, the last one was set at 1.5 mm from the punching edge. Gauge 10 was set at 0.5 mm from the punching edge.

For square metal plate specimens, gauges 1-5 were stuck on the metal plate with respect to the median direction and gauges 6-9 with respect to the diagonal direction. For $L = L_{TI}$ and $L < L_{TI}$ the spacing between two consecutive gauges was 1.5 mm and the last one was set at 1.5 mm from the punching edge. For $L > L_{TI}$ and for the diagonal direction, the last gauge was set at 1.5 mm from the punching edge but there was a 3mm space between two consecutive gauges. For all specimen lengths, gauge 10 was stuck on the metal plate with respect to the diagonal direction and was set at 0.5mm from the punching edge.

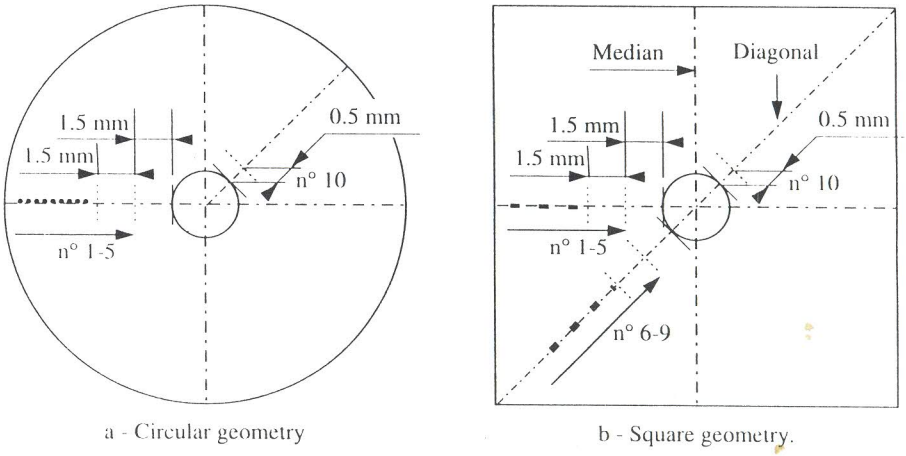

a - Circular geometry

b - Square geometry.

Figure 4 *Specimens instrumentation.*

The effective position of each gauge was fixed with an electronic microscope. Gauge instrumentation of the circular and square specimens (where $L = 20$ mm) is presented in Figure 5.

For all specimens, only the results of gauges which had similar positions when compared to the punching edge, are mentioned in Tables 2 and 3. This allows a better interpretation of results.

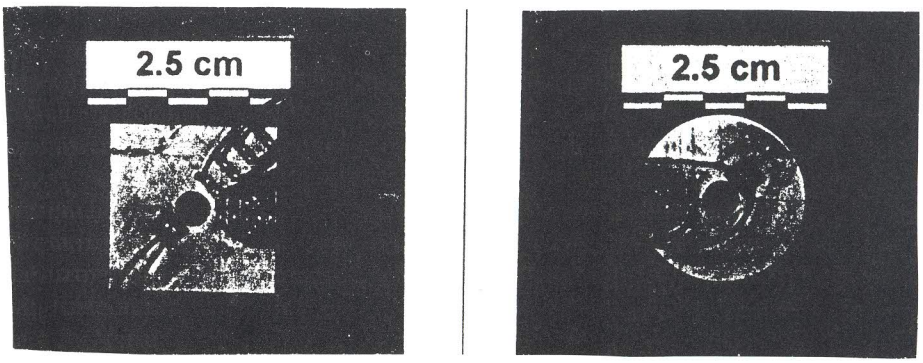

Figure 5 *Square and circular metal plate geometry specimen instrumentation.*

2.2 *Edge margin effects*

Table 2 summarises the experimental strain results for the circular metal plate geometry specimens according to the initial position of gauge δ_j, in terms of maximum and residual strains, ε_{max} and ε_{res}.

Table 2 Strain results of the circular metal plate geometry specimens.

N°	$\phi/2$ (mm)	L/2 (mm)	N° gauge	δ_j (mm)	ε_{max} (%)	ε_{res} (%)
1	2	10	3	4.3	-0.04	-0.04
			4	2.8	-0.10	-0.06
			5	1.3	-0.74	-0.70
			10^{-1}	0.5	> -20	/
2	2	7.5	1	4.3	-0.08	-0.07
			2	3	-0.15	-0.14
			3	1.6	-0.52	-0.51
			10^{-1}	0.45	> -20	/
3	2	5	1	1.4	-0.63	-0.63
			10^{-1}	0.6	> -20	/

[1] Gauge failure before the end of the test

An important strain gradient can be observed. Strain levels near the punching edge ($\delta j = 0.5$mm) are higher than 20%. For $\delta j > 1.5$ mm, strains levels are lower than 1%. Figure 6 presents the maximum strain state for the three specimens. Two phenomena can be observed:

(i) the first one reveals a strain increase near the punching when the plate diameter increases (more important strain localisation),

(ii) the second one corresponds to a strain homogenization when the plate diameter decreases.

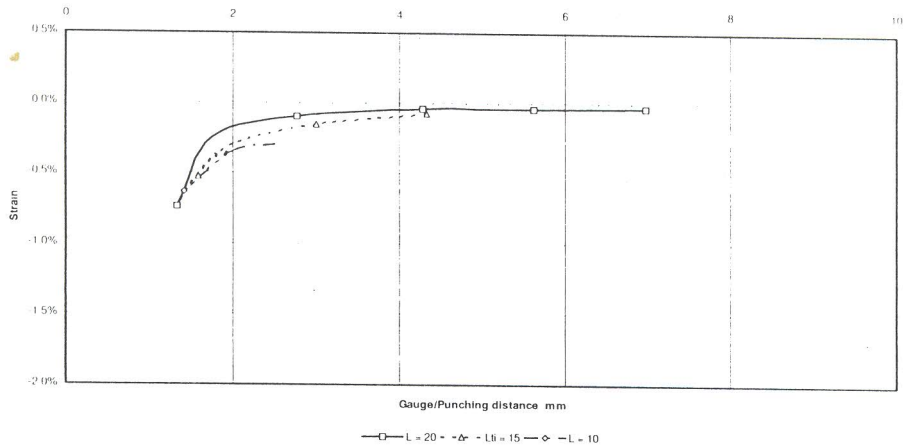

Figure 6 *Strain distribution of the circular metal plate geometry specimens.*

Table 3 Strain results of the square metal plate geometry specimens.

N°	ϕ/2 (mm)	L/2 (mm)	N° gauge	δ_j (mm) Median	δ_j (mm) Diagonal	ε_{max} (%)	ε_{res} (%)
4	2	10	1	7.3		-0.02	-0.02
			3	4.4		0.05	0.02
			5	1.3		-1.08	-1.00
			7		7.1	-0.01	-0.01
			8		4.3	-0.04	-0.04
			9		1.3	-0.49	-0.47
			10 [-2-]		0.6	> -20	/
5	2	7.5	1	4.4		0.02	0.01
			2	2.9		0.11	0.04
			3	1.3		-0.35	-0.28
			7		4.3	0.04	0.00
			8		2.8	-0.10	0.00
			9		1.4	-0.55	-0.48
			10 [-2-]		0.5	> -20	/
6	2	5	1	1.3		-0.26	-0.22
			6		2.7	-0.08	0.04
			7		1.3	-1.70	-1.63
			10 [-2-]		0.8	> -20	/

[-2-] Gauge failure before the end of the test

2.3 *Geometrical effects*

The synthesis of maximum and residual strains is given in Table 3 for each configuration. The riveting leads to an important strain gradient. Important strain levels (higher than 20%) can be observed near the punching (δ_j = 0.5mm). Strain levels are lower than 1% if they are further 1.5 mm from the punching edge.

The metal plate geometry effects (or corner effects) mainly concern the strain distribution between the median and diagonal directions. For the median direction, the strain distribution is very similar to the circular geometry (Figure 7):

(i) a *more important strain localisation* near the punching when the plate length *increases*,

(ii) a *strain homogenization* when the plate length *decreases*.

On the contrary, for the diagonal direction it can be observed that there is (Figure 8):

(i) a *more important strain localisation* near the punching when the *plate length decreases*,

(ii) a *strain homogenization* when the *plate length increases*.

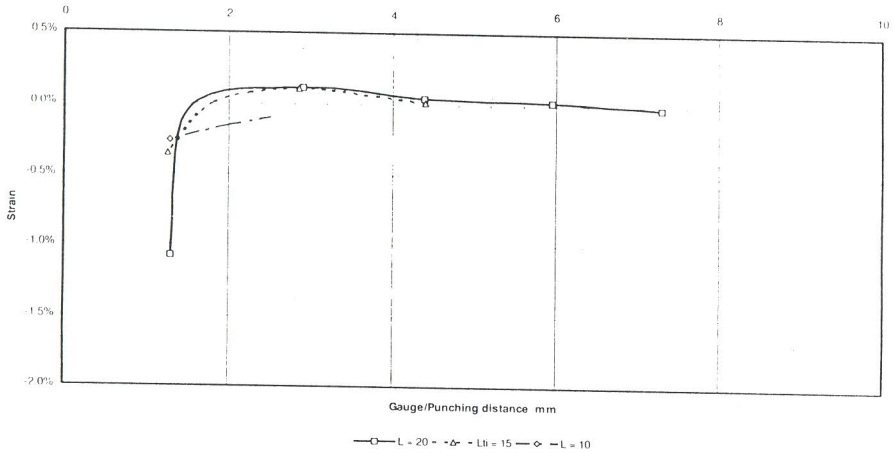

Figure 7 *Strain distribution of the square metal plate geometry specimens -Median direction-*

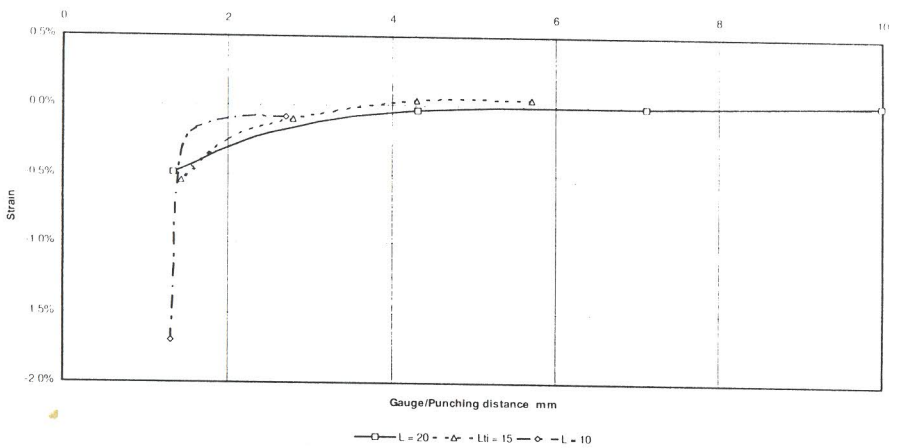

Figure 8 *Strain distribution of the square metal plate geometry specimens -Diagonal direction-*

2.4 Synthesis

The tests have shown high strain levels near the punching edge (a minimum of 20%). Edge margin effects have been studied by means of the circular metal plate geometry specimens. Two phenomena have been observed: greater strain localisation near the punching when the plate diameter increases and a strain homogenization when the plate diameter decreases. Geometrical or corner effects have been studied by means of the square metal plate geometry specimens. They concern essentially the strain distribution between the median and diagonal direction of the square geometry metal plates. However the dimension recommended by the calculation rules [3], $L = 15$ mm, constitutes the best case ($\varepsilon \leq 0.5\%$ for δ_j (mm) ≥ 1). For the two others ($L > L_{TI}$ and $L < L_{TI}$), the strain distribution is clearly unbalanced between the median and diagonal

direction of the square geometry metal plate specimens. In both cases, the circular metal plate geometry represents a medium state between the two directions of the square metal plate.

The extrapolation of some strain isolines illustrates a different behaviour between the two directions of the square geometry metal plate according to the specimen length (Figure 9). This distribution seems to reveal a more isotropic strain behaviour whatever the direction for $L = L_{TI} = 15$ mm (Figure 9(a)). For the two others ($L = 10$ mm and $L = 20$ mm) the strain distribution is more complex (Figure 9(b)-(c)). A preferential strain direction can be observed which may lead to material embrittlement.

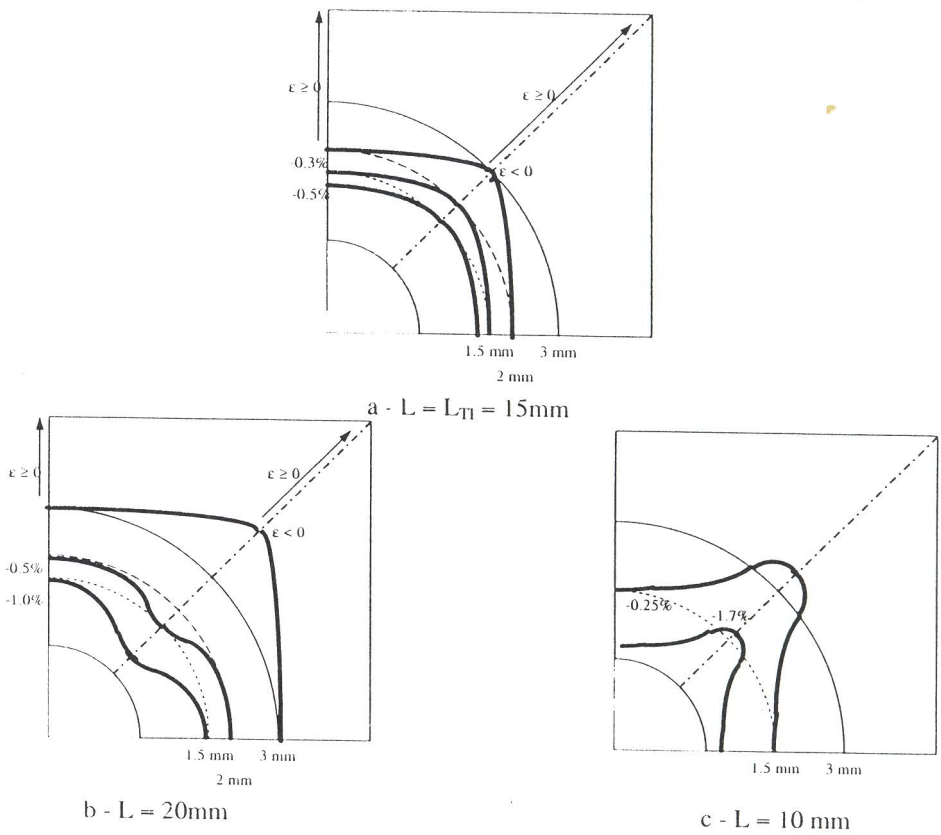

Figure 9 *Strain distribution - Isoline extrapolation.*

3 Riveting process analysis

Strength vs. time and strain vs. time diagrams show that the riveting process can be divided into seven distinct steps (e.g. diameter 20 mm - circular geometry metal plate, Figure 10). Figure 11 illustrates each step.

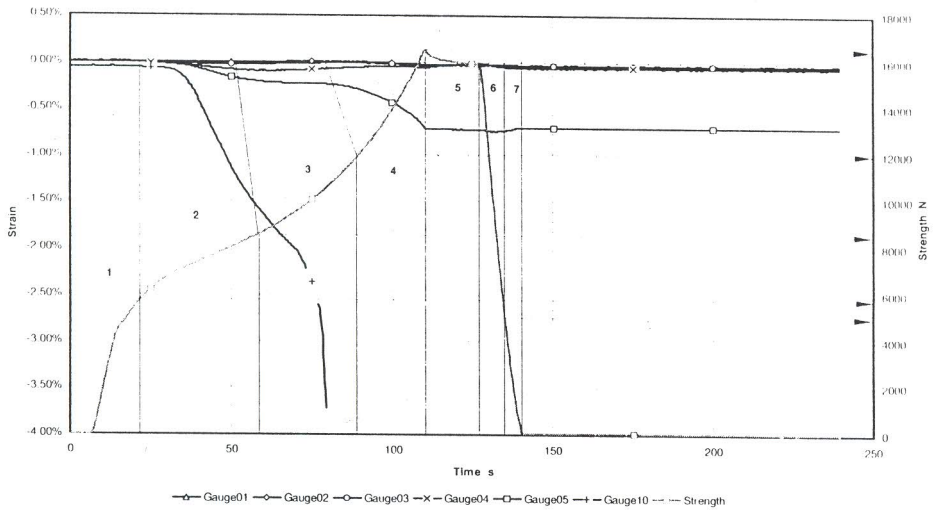

Figure 10 *Riveting steps.*

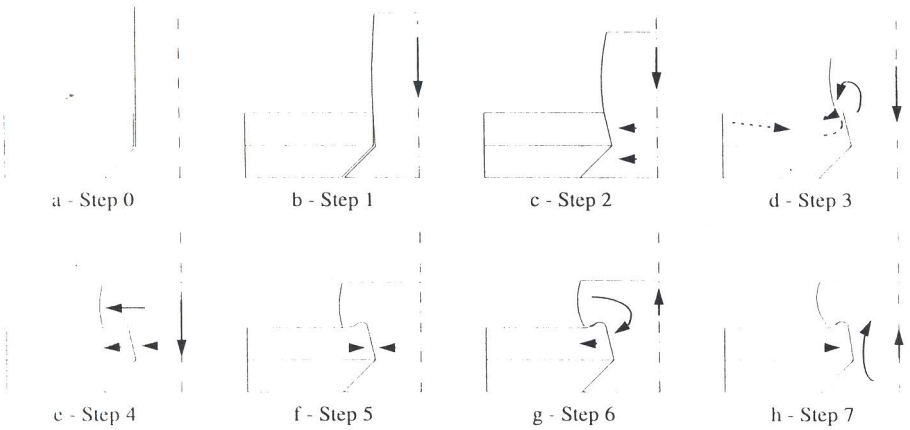

Figure 11 *Riveting mechanisms.*

(i) Step One: the strain gauge signals remain in their initial state. Strength increases and the rivet yield stress is exceeded.
This step corresponds to the crushing of the rivet only. It ends when the rivet touches the punching edges. This contact is detected as a compression signal by the strain gauge no. 10.

(ii) Step Two: all the strain gauges highlight a radial compression state of the metal plate. The contact area grows larger around and along the rivet shank until strength homogenization in the metal plate thickness. The driven head, upset rivet part, can be formed.

(iii) Step Three: the radial compression signal given by the gauge no. 10 becomes more pronounced. At the same time the signal of the other gauges far from the punching are reversed to reveal a pseudo-tension. Strains above 20% are recorded during this step by the gauge no. 10. This gauge is destroyed during this step.
The driven head forms. It comes into contact with the metal plate area of the specimen. Friction in this contact area introduces a new material flow: a *lug*, trapped by the rivet driven head, is forming near the punching. For the gauges far from the punching, it leads to a reversed signal and a metal plate tension state.

(iv) Step Four: the strain gauges signal shows a new radial compression of the metal plate. The lug is completely formed. The rivet driven head forming continues.

(v) Step Five: the rivet driven head dimensions are attained. The displacement of the compression machine cross bar is stopped until the strength homogenization (fifth step). The maximum strength in the order of 16300 N decreases to keep stable (15700 N).
This transitional step corresponds to a homogenization of the interface stresses between the rivet and the metal plates (contact between the rivet driven head and the metal plate, contact between the rivet shank and the punching).

(vi) Step Six: the compression machine cross bar goes up. Strength decreases. The rivet driven head remains in contact with the cross bar. Strain gauges show a new metal plate radial compression.
This is due to the rivet driven head (the most deformed part of the rivet) making its elastic return. It releases some strength into the rivet shank which sends a new radial compression strength to the metal plates.

(vii) Step Seven: the cross bar goes up. Strain gauges' signals are reversed and show a state of tension. This last step ends when the strength comes back to zero. This phenomenon corresponds to the metal plate partial elastic return. This phenomenon is possible if the rivet shank is partially unloaded.

The riveted joint obtained is well balanced. Strain gauges then show the residual strain state of the metal plates. Figure 12 presents the lug described in Step Three. The strength and displacement of each step are repetitive for all the tests (for each metal plate dimension) and show that the seven steps are representative of the rivet forming process.

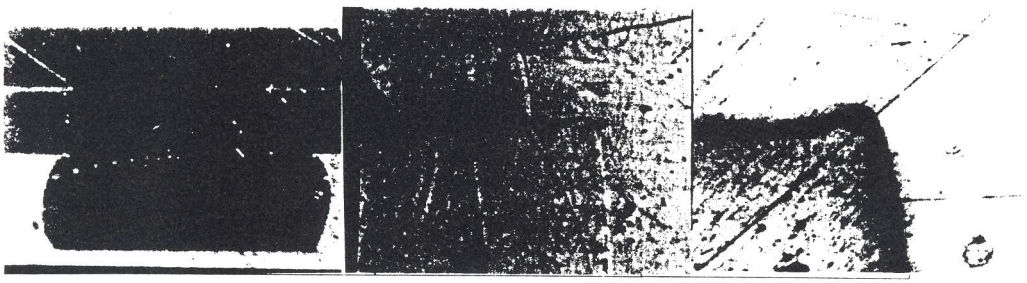

Figure 12 *Experimental visualisation of the lug.*

4 FE modelling of the riveting process

The objective of this study is not to simulate all the experimental tests. The aeronautical frameworks are thoroughly checked to ensure that the nominal pitch or edge margin are respected. The cases $L > L_{TI}$ and $L < L_{TI}$ should therefore not occur in such frameworks. An FE model is carried out for a square metal plate geometry and for the joint dimensions recommended by the calculation rules [3].

Only a quarter of the specimen is modelled for obvious reasons of symmetry and computing cost. The bed and the cross bar head of the compression machine are represented by two rigid walls. Rigid walls are chosen as infinite planes with infinite mass and finite friction ($f = 0.2$, default value for metal/metal contact). The first one is fixed. The second one crushes the rivet (a moving one).

A sensitivity study was undertaken for the crushing velocity to limit computing cost. It shows that inertia and wave propagation effects are limited until the crushing velocity is in the order of 10 m/s. The crushing step can then be performed with a 10 m/s velocity without any differences when compared to the quasi-static behaviour. The velocity curve of the moving rigid wall is presented in Figure 13. The velocity curve is, like the experimental curve, divided into three steps: a crushing one for $0 \le t(\text{ms}) < 0.28$ with 10 m/s imposed velocity, an homogenisation one for $0.28 \le t(\text{ms}) \le 0.30$ with a zero imposed velocity and a relaxation step for $0.30 < t(\text{ms}) \le 0.50$ with a negative imposed velocity (–10m/s).

The elastic and plastic mechanical properties of the 2024-T351 and 7050 aluminium alloys are given in Table 4 [9]. Dynamic tests have revealed no strain rate sensitivity for these two materials [9]. The identification of the true stress vs. true plastic strain diagrams by an inverse method [10-11] has given the power constitutive model parameters (1) of the two aluminium alloys [9]. The shear and bulk moduli are calculated by (2) and (3).

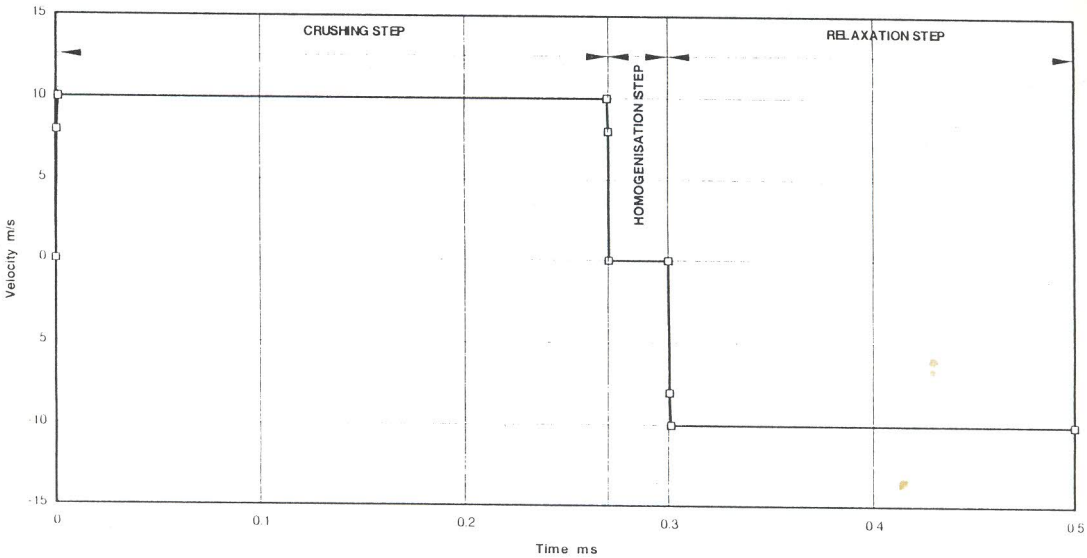

Figure 13 *Moving rigid wall velocity curve.*

Table 4 Elastic and plastic mechanical properties.

Aluminium alloy	E (GPa)	ν	ρ (g/mm^3)	G (GPa)	K (GPa)	A (GPa)	B (GPa)	n
2024-T351	74	0.33	0.0028	27.82	72.55	0.3052	0.3053	0.1461
7050	74	0.32	0.0028	28.03	68.52	0.3125	0.2905	0.2503

$$\sigma = \left(A + B \cdot \varepsilon_p^n\right) \tag{1}$$

$$G = \frac{E}{2 \cdot (1+\nu)} \tag{2}$$

$$K = \frac{E}{3 \cdot (1-2 \cdot \nu)} \tag{3}$$

The metal plates and the rivet are modelled with elastic-plastic solid elements (type 1 in PAM-SOLID™ standard [12]). The contact between the rivet and the punching, and between the two metal plates, is controlled by a self impacting contact interface (type 36) with a finite friction ($f = 0.2$). With this contact interface, friction is modelled with a Coulomb model (4). This bounded friction model expresses the tangential stress σ_{12} (which is opposed to the translatory motion) as a function of the normal stress σ_{11}. This kind of model assumes a fixed finite friction, f.

$$\sigma_{12} = f \cdot \sigma_{11} \tag{4}$$

The FE model is made up of six solid elements across each plate thickness which gives a better representation of the local phenomena observed in the metal plate thickness. The FE model is finally made up of 14177 solid elements and 17362 nodes. The FE model, at the initial and final time step, is presented in Figure 14. The computing time of this FE model is in the order of 10 hours on a J90 CRAY supercomputer with four processors.

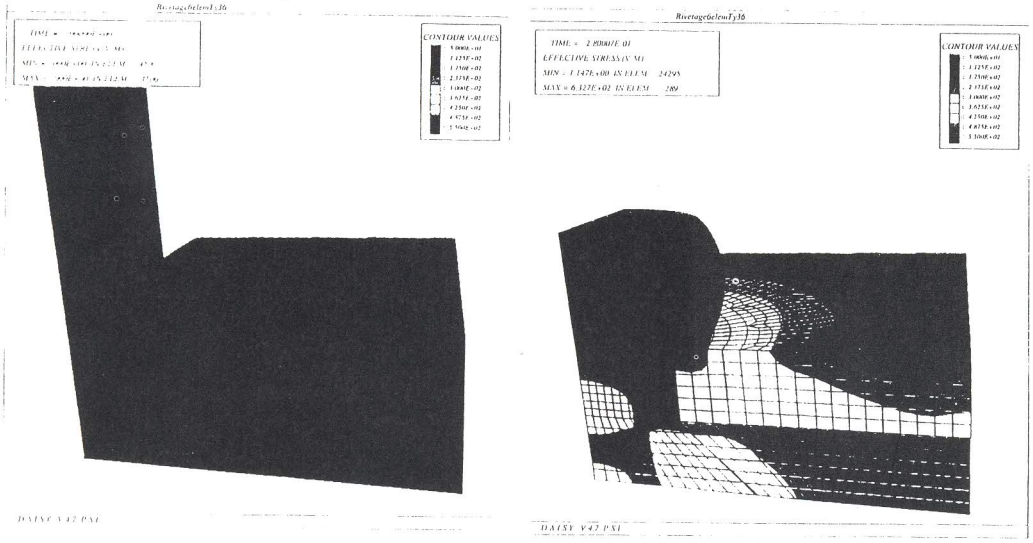

a - Initial time step b - Last time step

Figure 14 *FE model deformed shape (with 6 solid elements across each plate thickness).*

The FE model's results are globally and locally compared with the experimental results. The strength vs. crushing displacement diagram is shown in Figure 15. The strength vs. metal plate local strain diagrams are shown in Figures 16 and 17 for $\delta_j = 1.5$mm in the median and diagonal directions and Figure 18 for $\delta_j = 0.5$mm in the diagonal direction.

The FE model leads to a rivet driven head with a 6mm diameter and a 2.2mm height (Figure 19) which is in accordance with the margin imposed by the table from [6] and the experiment (Table 5). Figure 15 shows a good correlation between the numerical and experimental results according to the strength vs. crushing displacement diagram. The maximum gap between the FE model and the experiment is lower than 5% for a crushing displacement limited between 1.5 and 2mm. The gap at the maximum strength is lower than 4%. These results prove the validity of the FE model's parameters.

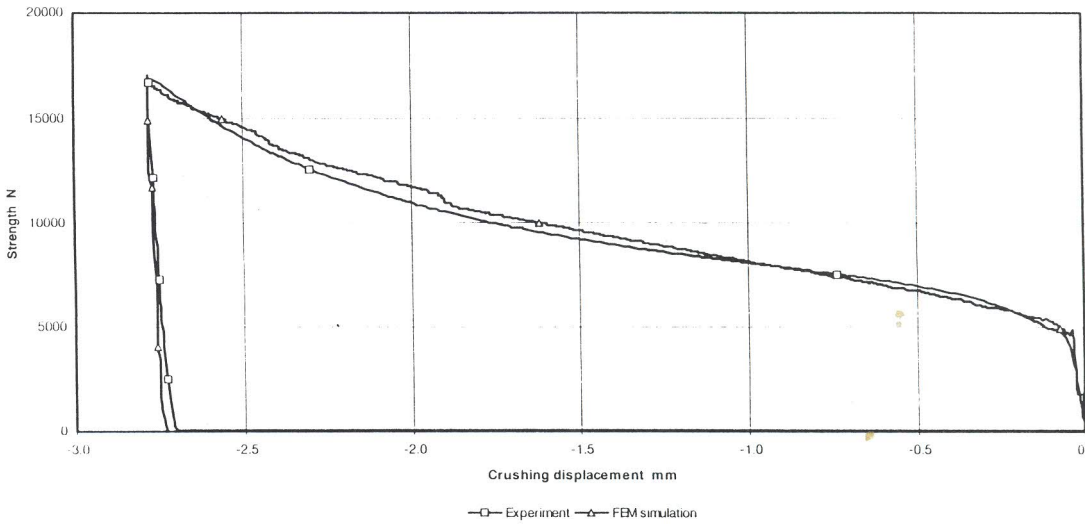

Figure 15 *Strength vs crushing displacement diagram.*

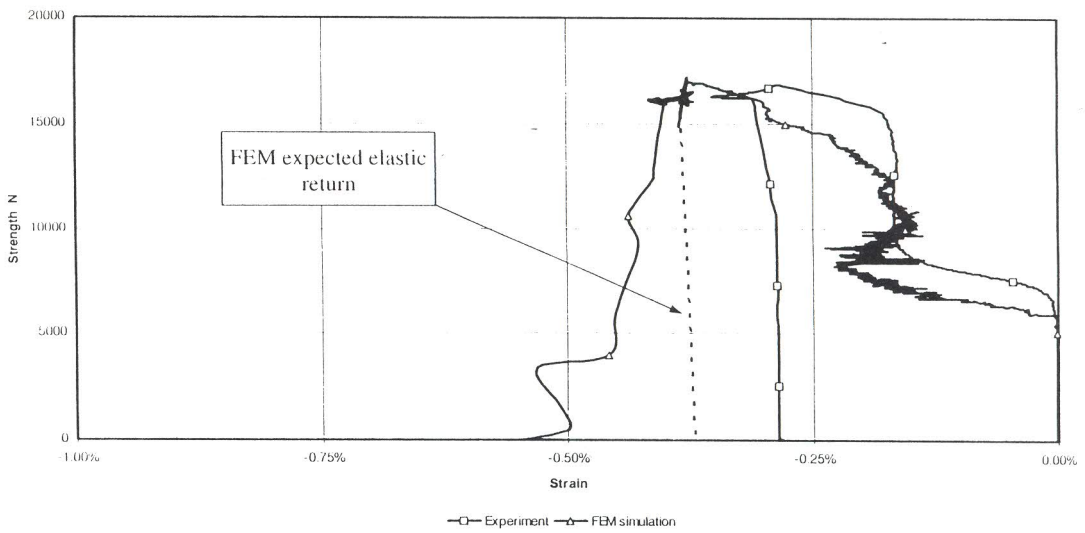

Figure 16 *Strength vs. metal plate local strain diagram (δ_j = 1.5mm - Median direction).*

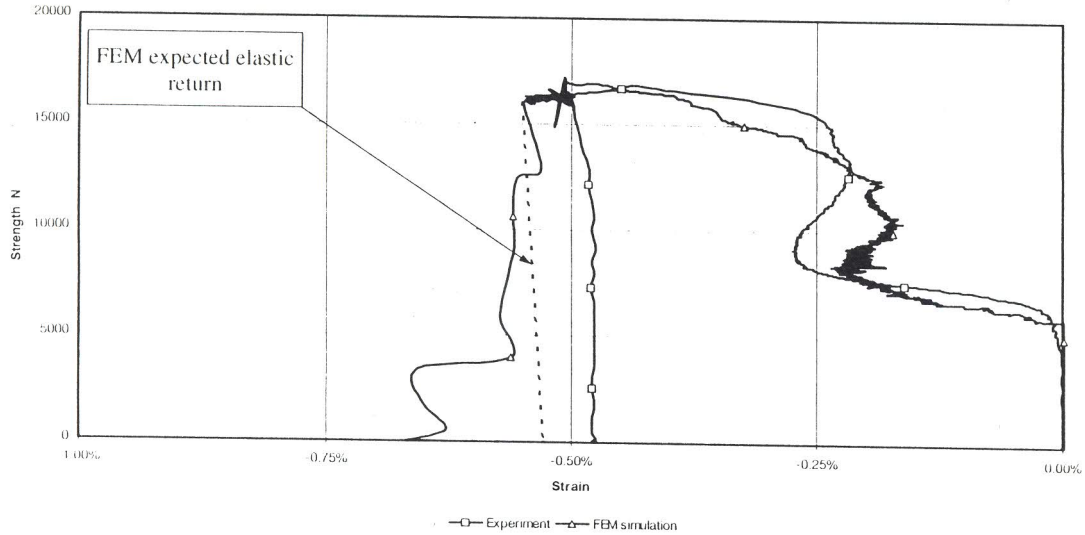

Figure 17 *Strength vs. metal plate local strain diagram (δ_j = 1.5mm - Diagonal direction).*

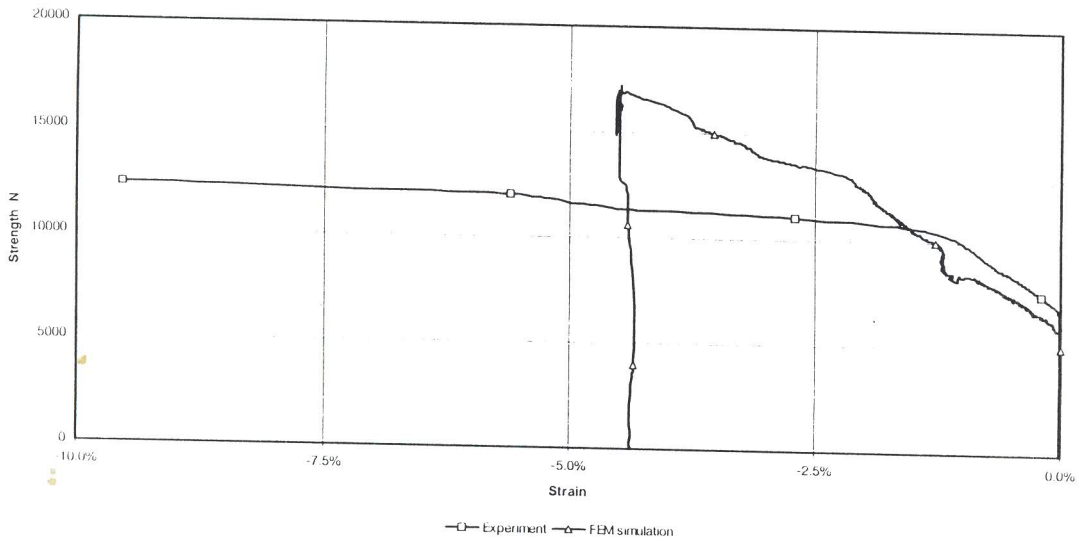

Figure 18 *Strength vs. metal plate local strain diagram (δ_j = 0.5mm - Diagonal direction).*

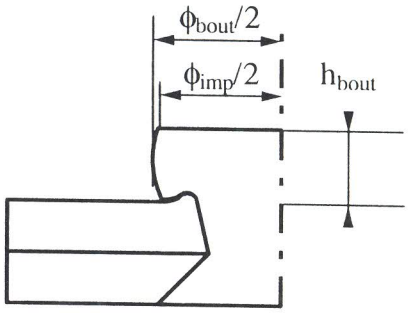

Figure 19 *Rivet driven head dimensions.*

Table 5 Comparison of rivet driven head dimensions for FEM, table and experiment.

Driven head property	FEM (mm)	Norm [6] (mm)	Test -mean values- (mm)
h_{bout}	2.20	≥ 1.19	2.20
ϕ_{imp}	5.50	≥ 5.15	5.70
ϕ_{max}	6.08	≤ 6.70	6.15

The local results in terms of strength vs. local strain diagrams are representative of the material flows experimentally measured (tension returns due to the lug creation). Moreover, the mesh refinement predicts the general trend of the strain distribution between the median (Figure 16) and the diagonal (Figure 17) directions. FE results show that the maximum strain at 1.5 mm from the punching edge is attained for the diagonal direction which is in line with experiments.

The differences of the residual strains (compared to the elastic return expected according to the dotted lines, in Figures 16 and 17) are principally due to a significant relaxation velocity of the moving rigid wall. This significant velocity introduces an oscillatory behaviour of the strain response which can be eliminated by the introduction of mass nodal damping. The numerical residual strains for the gauges at 1.5mm from the punching are slightly higher when compared to the experiment. Near the punching ($\delta_j = 0.5$mm) the numerical strains are lower than those measured (Figure 18). The strain level at the punching edge depends on the strength in the contact area. It has been shown that different contact control methods lead to the same numerical results [13].

The differences between the FE model and the experiment can therefore come from:

(i) the mesh refinement,

(ii) the plastic strain localisation which depends on:

- the metal plate constitutive model,
- the friction parameter of the contact interface.

The calculation of two new FE models with and without contact interface friction (12 solid elements across each metal plate thickness, computing time in the order of 20 hours) dismisses the first hypothesis (mesh refinement). Even if the local results are improved at 1.5 mm from the punching edge with friction (Figure 20), this new model does not come close to the real local results observed at 0.5mm from the punching edge. Figure 21 (where the dotted lines represent trend curves) presents the strain state observed from $\delta_j = 0.085$ mm to $\delta_j = 1.5$ mm. The strain distribution is obviously non linear. A maximum strain can be observed near the punching (but not at the edge) and a second one for $0.5 < \delta_j$ (mm) < 0.7 (Figure 20). This type of distribution does not correspond to the experimental results (strain decreases in a exponential way).

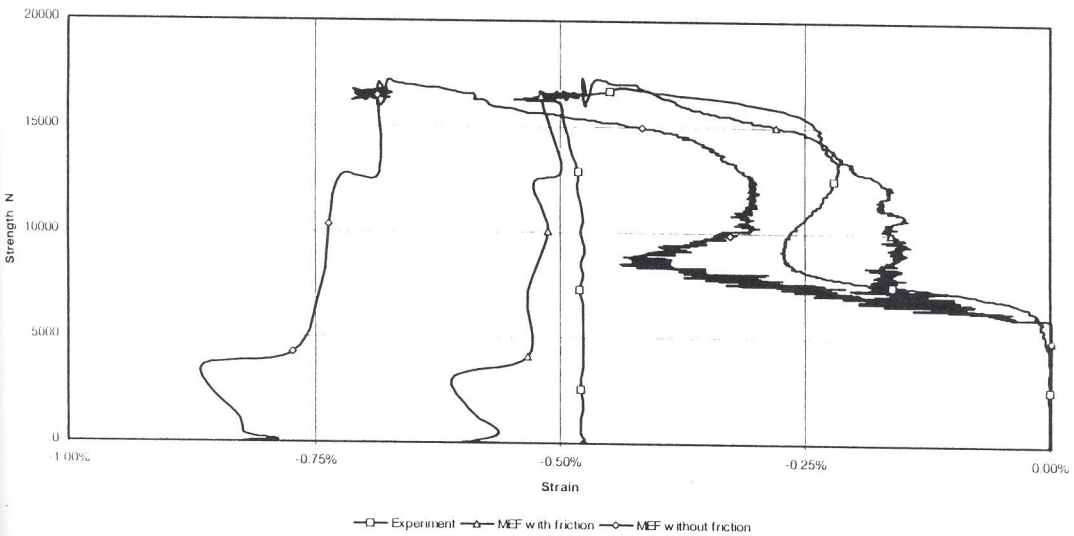

Figure 20 *Friction sensitivity (FE model with 12 solid elements across the metal plate thickness).*

The numerical plasticity near the punching depends naturally on intrinsic material parameters (E, ν, $\sigma(\varepsilon^p)$) and on an environmental parameter: the contact interface friction. This parameter, fixed at 0.2 since the beginning of this study, influences the plasticity as soon as the contact occurs between the rivet and the punching. The FE simulation without contact interface friction allows one to evaluate the sensitivity of this parameter. Results show that its influence takes place essentially near the punching (Figure 21). The FE model without friction is less representative for the residual strains. However, at the beginning of the riveting process the behaviour seems to be better (Figure 20). The tension return is more pronounced without friction when compared to the case with friction. A new FE calculation with an intermediate value of friction wasn't undertaken. The problem only derives from the bounded friction model. The Coulomb model is not suitable for a realistic prediction of the friction stress for high levels of the contact pressure.

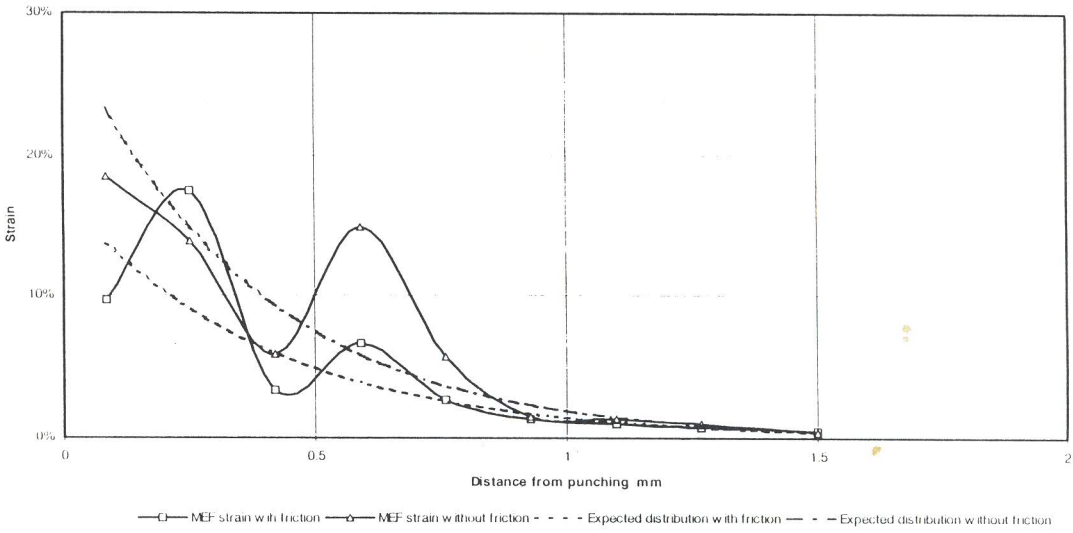

Figure 21 *Strain distribution with or without contact interface friction.*

Figure 22 presents the simulated plastic strains near the punching for the two contact interface frictions. It shows the influence of this environmental parameter on the local result. The contact interface friction has however a minor influence on the riveting process behaviour (Figure 23).

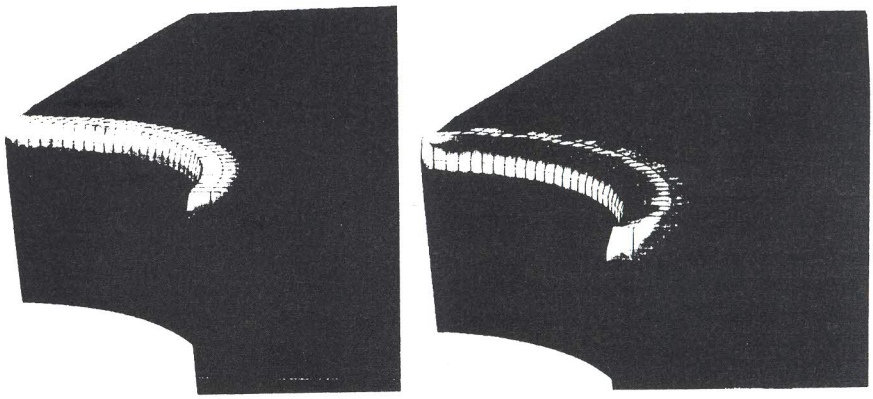

a - Without contact interface friction b - Contact interface friction : 0.2

Figure 22 *Local influence of contact interface friction.*

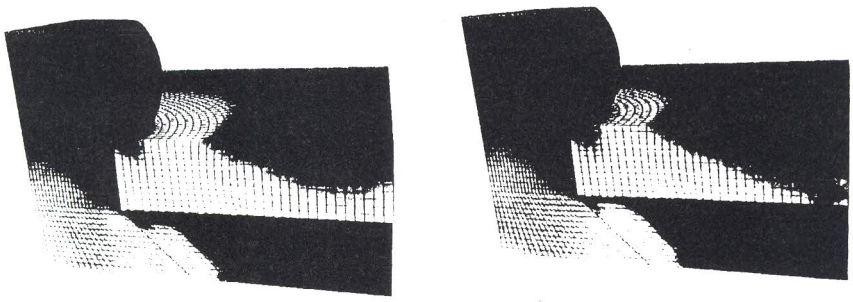

a - Without contact interface friction b - Contact interface friction : 0.2

Figure 23 *Global influence of contact interface friction.*

5 Conclusion

This paper deals with the experimental and numerical residual strains inside riveted specimens as a result of the joining process. Experiments were carried out on simple circular and square metal plate specimens, varying the nominal edge margin from ±30% ($a/\phi = \{1.5,\ 1.875,\ 2.5\}$). The influence of the edge margin to rivet shank diameter aspect ratio was measured through experiments on circular metal plate geometries (isotropic strains). Results show the influence of this aspect ratio on the strain localisation and distribution. Geometrical or corner effects were also measured by means of the square metal plate geometry specimens. Results show different residual strains for the diagonal and the median directions. The results observed for the circular geometry seem to give a medium state between the two directions of the square specimen. The riveting process gave rise to a significant strain gradient characterised by strains above 20% at 0.5mm from the punching edge. However the dimensions recommended by the calculation rule, that is to say $a/\phi = 1.875$ constituted the best case. The detailed analysis of the joining process has shown that the riveting can be organised into seven distinct steps. Each step corresponds to different energy transfers between the rivet and the metal plates. This analysis has revealed a material lug creation.

A secondary aim was to accurately model the joint and evaluate the simulation capability by explicit FE codes such as PAM-SOLID™ to represent the local material flows due to the riveting process. The FE simulation leads to satisfactory results in terms of strength vs. crushing displacement and strength vs. local strain diagram when compared to experimental results. The lug is not correctly represented by the FE model in spite of the mesh refinement. The tension return is however represented on the strength vs. local strain diagrams. The influence of the contact interface friction

specifications are clearly seen. The FE model's results illustrate the insufficiency of bounded friction models such as the Coulomb model.

The FEM results nevertheless prove the simulation capability of the numerical tool to represent this complex forming process. They allow one to undertake other research themes linked to the joint quality improvement (e.g. punching burring problem before riveting) or the calculation rules rationalisation applied to composite frameworks (e.g. edge margin, pitch, initial damage). FEM numerical tools can therefore optimize rivet designs move quickly and cheaply than experiments. FEM simulation nevertheless estimates the local behaviour (material flows) more quickly. The residual stress and strain prediction by FEM simulation can be considered as the initial state for the new FE simulation of the mechanical resistance of riveted assemblies.

Acknowledgement

This research was carried out with an ONERA grant (operation numbers 96211 and 97207) under the responsibility of Dr. P. GEOFFROY, assistant manager of the ONERA/MSE department and in charge of the DMSE/RCS section. The authors are grateful to the ESI Group for the PAM-SOLID™ FE code and we wish to especially thank Dr. X. NI and P. CULIÈRE for their suggestions. The authors also wish to thank the DASSAULT AVIATION Company.

References

1 Deletombe, E. (1996) 'IMT crashworthiness for commercial aircraft. Finite element modelling of joints, plastic buckling and failure - Final report', *ONERA-Lille Report n°96/25*.

2 Deletombe, E. and Malherbe, B. (1997) 'Simplification d'un modèle de crash d'avion complet - Phase 1- Rapport final', *ONERA-Lille Report n°97/02*.

3 Charlier, J. (1981) 'Fonction immobilisation: Agrafage, sertissage, rivetage', *Engineering Technical*, n°B5-535, pp. 1-19.

4 US Military standard (1986) 'Rivets, buck type, preparation for and installation of', MIL-R-47196A-NOTICE 1.

5 Bruhn, E. F. (1973) *Analysis and design of fight vehicle structures*, Jacobs Publishing. Inc.

6 US Military standard (1992) 'Military standard, preparation for and installation of', MIL-STD-403C-14.

7 Moutier, D. and Galkovsky, N. (1993) 'Détection et analyses de déformées de faibles amplitudes', DASSAULT AVIATION, *Technical General Direction Report n°53.939*.

8 Olsson, R. (1990) 'Pilot study of the dynamic impact response of a composite plate', *Report FFA TN 1990-27*.

9 Langrand, B. (1997) 'Experimental characterisation of 2024-T351 and 7050 aluminium alloys', *ONERA-Lille Technical note n°97/54*.

10 Langrand, B. (1997) 'Development and validation of parametric identification methods - Evolution to an inverse method', *ONERA-Lille, Technical note n°97/51*.

11 Langrand, B., Markiewicz, E., Drazetic, P., Geoffroy, P., Petitniot, J. L. and Fabis, J. (1997) 'Constitutive models characterisation for XC48 steel in compression by a parametric

identification technique', *Int. J. of Materials and Product Technology*, Vol. 12, Nos. 4-6, pp. 428-446.

12 PAM-SOLID™ (1996), *User's manual*, ESI-PSI, 20 rue Saarinen, Silic 303, 94588 Rungis cedex, France.

13 Langrand, B. and Deletombe, E. (1998) 'Riveted assemblies embrittlement - Validation of riveting process by finite elements models', *ONERA-Lille, Technical note n°98/02*.